

A Spectroscopic Study of the Variable Star T Centauri Over a 91-day Cycle, and the Effects of Titanium Oxide on Its Atmosphere

Julian F. West

Astronomical Association of Queensland (AAQ), P. O. Box 6101, St. Lucia, Queensland 4067, Australia; spectroscopy@aaq.org.au

Benedict Pace

54 Bowley Street, Hendra, Queensland 4011, Australia; ben_penny1@bigpond.com

Received November 9, 2020; revised March 7, 2021; accepted March 15, 2021

Abstract We observed spectra of the large amplitude semiregular variable T Centauri during a complete 91-day period, which were subsequently combined with contemporaneous photometric data from the AAVSO International Database. The analysis of these data, together with other reference material, has enabled us to estimate a mean photospheric radius of T Centauri at $\sim 94 R_{\odot}$, and to develop a simple model reflecting the effects of the formation of titanium oxide in the star's atmosphere as it cools through minimum brightness. Our model incorporated the variation in atmospheric opacity due to TiO and, in comparison with the observed magnitudes, indicated an increase of 20–40% in the apparent stellar radius, as observed in the visual and near-infrared bands as the star cooled mid-phase.

1. Introduction

Miras and other large amplitude semiregular variables have long periods of between 100 and 1,000 days, and visual amplitudes of at least 2.5 magnitudes, but in some cases up to 10 magnitudes (Percy 2007). They are enormous stars, with radii often extending to ~ 2 AU, or several hundred solar radii. They are also cool, generally of spectral type M, and metals in their extended atmospheres can form molecules such as titanium oxide (TiO) and vanadium oxide (VO) as they cool towards minimum light. This has been described as creating a “visual surface” far above the true stellar surface—the photosphere—if the optical depth is sufficiently great and can therefore affect the apparent radius of the star (Reid and Goldston 2002a, b). Our paper explores these issues for T Centauri based on extensive captured spectra, together with photometric data from the AAVSO's International Database of variable stars (Kafka 2020). These data have been used to estimate a mean photospheric radius of the star for the purposes of calculation (but for which little information was readily available), and to develop a simple model of the behavior of the complex atmosphere and the increase in the apparent “effective radius” related to the formation of atmospheric TiO.

Our broader project involves the examination of a number of southern Mira variable stars—which may not have been well studied by northern hemisphere astronomers—with a particular focus on their spectral variation and the effects of metallic oxides in their atmospheres. Ten Miras were selected with a broad range of period, magnitude, and spectral type, well spread out in Right Ascension, to permit observations throughout the year. Each candidate star was allocated a reference star, to enable an accurate determination of, and correction for, instrument response. T Cen was included as a candidate in this project as it is indicated as a Mira variable in the SIMBAD database (Wenger *et al.* 2000), although in the wider literature it is more commonly listed as a large amplitude semiregular variable, of type SRa (Lebzelter *et al.* 2005; Lançon and Mouhcine 2002); it is also listed by the AAVSO

as a form of RV Tauri semiregular variable. Nevertheless, its visual amplitude regularly exceeds the 2.5-magnitude threshold specified by the *General Catalogue of Variable Stars* (GCVS; Samus *et al.* 2017) for inclusion as a Mira. Its amplitude in spectral type is similar to that of other Miras, such as S Car, X Men, and SW Hya, whereas its spectroscopic behavior beyond $1\mu\text{m}$ reinforces the SRa classification (Lançon and Wood 2000). These potentially mixed characteristics leave T Cen as an interesting object whose behavior we have tried to model within the scope of our available data, and which may in turn facilitate interesting comparisons with other Mira variables within our study.

2. Observations

2.1. Spectra

The spectra of T Cen were captured at the Hendra, Queensland, observatory located at latitude 27.42° S and longitude 153.06° E, at an altitude of 26 m. The instruments used were a Takahashi 180ED telescope on an EM200 mount, equipped with a $2\times$ Barlow and a Spectra 200 Littrow slit spectrograph manufactured by JTW Astronomy. The spectrograph was equipped with a grating of 600 lines/mm, giving $R\sim 2000$. Spectra were recorded on an Atik 383L+ monochrome CCD camera, cooled to -10° C. The grating was set to record a wavelength range of $\lambda\lambda 6400\text{--}7600$, with multiple 10-minute subframes captured to ensure a signal to noise ratio of at least 50 when the star was at minimum. Wavelength calibration spectra were captured using an integrated neon source, and corresponding spectra were also recorded for the nearby designated reference star, ι Cen (A2 V), at each observing session.

The captured spectrograms were processed using the software program ISIS: Integrated Spectrographic Innovative Software, developed and supported by Christian Buil (Buil 2019). This program simplifies the processing of spectra, and applies flat fields, master bias, dark, and “hot pixel” frames and takes account of tilt and slant occurring in the recorded

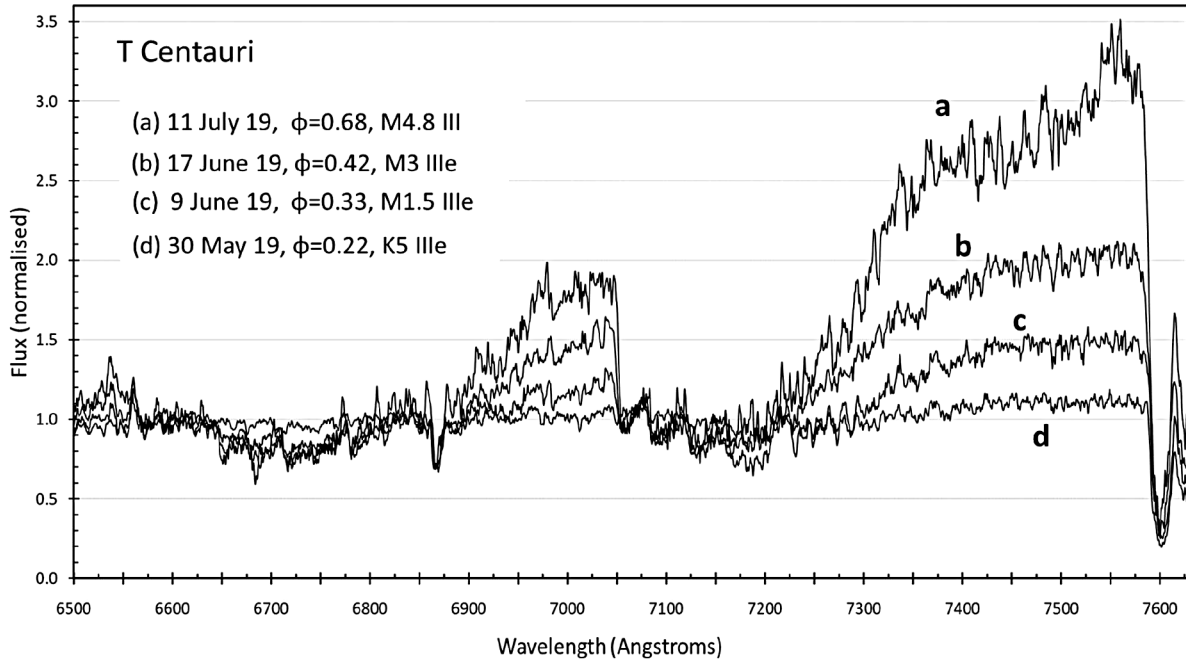


Figure 1. Example captured spectra, normalized at $\lambda 6610$; the legend shows phase and spectral type, illustrating both maximum light in May 2019 and minimum light in July 2019.

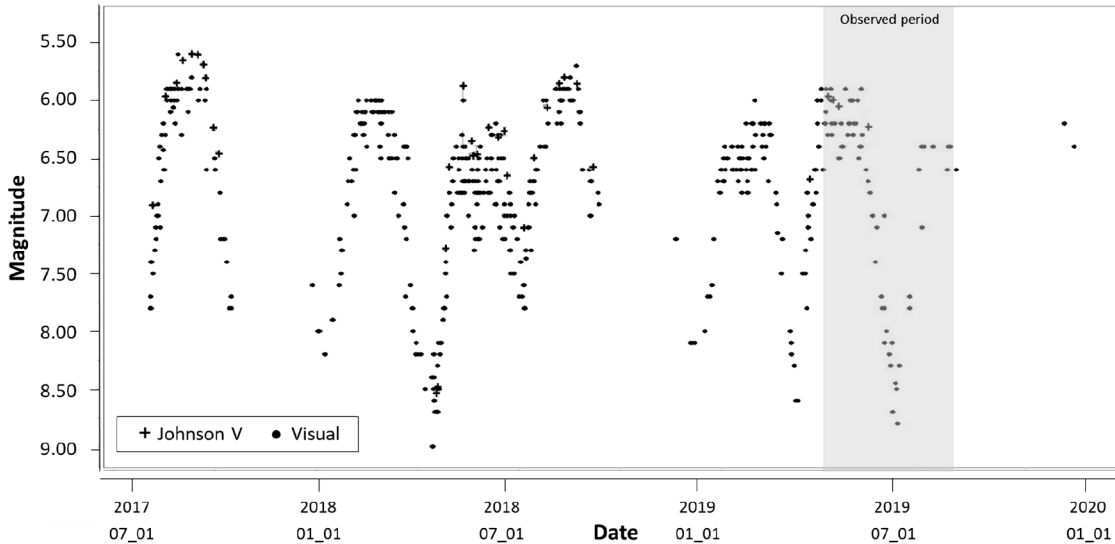


Figure 2. Observed apparent magnitude m_v of T Cen from July 2017 to the end of 2019; the shaded section is the period of observations used in this paper (from the AAVSO International Database, Kafka 2020).

spectrograms. It also applies the instrument response correction derived from the reference star and normalizes the target spectra at the specified $\lambda 6610$. Examples of the captured spectra are compared in Figure 1, and profiles of all spectra referenced in the tables are also shown in the Appendix. In addition, original copies of these spectra in .fit format may be accessed through the AAVSO ftp site at

<ftp://ftp.aavso.org/public/datasets/west491-fitspectra.zip>.

We classified the spectra visually using the XCLASSMIRA program, adapted from the XCLASS and MKCLASS programs of Professor R. O. Gray (Gray and Corbally 2014). XCLASSMIRA provides classification capabilities at the red end of the visual spectrum (as opposed to the more conventional blue end used

by XCLASS), better suited to cooler stars, and uses a library of reference spectra developed at the Astronomical Association of Queensland (AAQ) for that purpose.

2.2. Photometric data

We did not observe T Cen photometrically during the spectroscopy observations. We therefore referred to the extensive resource provided by the American Association of Variable Star Observers (AAVSO), which offers a long historical record of apparent magnitudes of variable stars including T Cen. However, these observations are mostly visual and commonly vary by ± 0.25 mag (or more) so some interpretation was required. The AAVSO record of observed m_v for T Cen over

an extended period is shown in Figure 2, illustrating a regular amplitude in m_v of well over 2.5 magnitudes, and its regular period of 90.7 days (Kafka 2020).

The apparent visual magnitude data available from the AAVSO has been used in section 3.3 to develop a set of bolometric magnitudes and luminosity values to compare with those calculated directly from the spectra themselves.

3. Analysis and results

By themselves, neither the captured spectra nor the observed magnitudes provided by the AAVSO gave a complete picture of the behavior of T Cen and its atmosphere throughout its period. Our analysis of the captured spectra, together with readily available reference data, was conducted in two stages: first, the expected luminosities and magnitudes were calculated, as outlined in section 3.1, for comparison with the observed magnitudes from the AAVSO. Second, the 18 key spectra represented in the tables and figures were rectified, setting the continuum at unity, to enable the absorption of light by the atmospheric TiO to be measured by wavelength across the cycle (section 3.2), to indicate the atmospheric optical depth. The calculated (expected) magnitudes from section 3.1 were then compared with the magnitudes and luminosities derived from the AAVSO's corresponding T Cen observations (section 3.3) to enable disparities to be identified. The reconciliation of these differences is discussed in section 3.4, together with an interpretation of the results, including estimates of the apparent "effective radius" of T Cen when affected by TiO during minimum light. The optical depth of the stellar atmosphere, derived from the absorption measurements, is also considered in this context and in the Discussion (section 4).

3.1. Captured spectra: calculation of magnitudes

Following data reduction of the captured spectra, 53 in total, 33 were selected to provide a thorough coverage of the spectral variations across the complete period, without undue repetition. These were then visually classified by spectral type using the `xCLASSMIRA` application and the AAQ's library of Mira reference spectra. In addition, the phase was calculated from the observation date, using ephemerides from the AAVSO, with the peak of the light curve on 2019 May 10 defined as phase zero and a period of 90.7 days. The standard effective temperature indicated by each spectrum was then sourced from "Appendix B: Calibrations of the MK System" (Gray and Corbally 2009). To enable a comparison with the photometric observations of the AAVSO, the spectral classifications and their corresponding MK temperatures (for giant stars) were used to calculate the expected luminosity and bolometric magnitude of T Cen for each spectrum, from which were derived absolute and apparent visual magnitudes. The classified spectral types, temperatures, and results are shown in Table 1, and an explanation of the calculations and assumptions follows. The results are plotted by phase in Figure 6 (in section 3.3), which also illustrates both the values observed by the AAVSO contributors and the revised calculated magnitudes resulting from the comparison.

Luminosity was calculated using the Stefan-Boltzmann formula:

$$L = 4\pi R^2 \sigma T^4 \quad (1)$$

where R is the stellar radius (m), T the temperature (K), and σ is the Stefan-Boltzmann constant ($5.67 \times 10^{-8} \text{ W} \cdot \text{m}^{-2} \cdot \text{K}^{-4}$).

Little information was readily available on the radius of T Cen; a value of $4.5 \times 10^{10} \text{ m}$ was adopted as a starting point, being $\sim 65 R_{\odot}$, obtained from Universe Guide (2020). The radius of a Mira has been shown to vary, and interferometric measurements at $11 \mu\text{m}$ of Mira (o Ceti) itself have indicated variations with phase of perhaps 10% (Weiner *et al.* 2003a, Figure 5). Measurements of the radial velocity of T Cen (Lebzelter *et al.* 2005) show variations from 24 km s^{-1} to 36 km s^{-1} , an amplitude of $\pm 6 \text{ km s}^{-1}$, inferring significant pulsation with the mean radius occurring at phase ~ 0.8 .

Luminosity is more dependent on temperature (at the fourth power), so the radius of the photosphere was assumed to be constant for the purposes of these initial calculations. Luminosity L (in Watts) may be converted into an absolute bolometric magnitude using the following equation:

$$M_{\text{bol}} = -2.5 \log (L/L_0) \quad (2)$$

where L_0 is the zero point of the absolute bolometric magnitude scale and is defined as the following value:

$$L_0 = 3.0128 \times 10^{28} \text{ W (Mamajek *et al.* 2015).$$

Bolometric conversion factors (Kaler 1989), BC_v , which are dependent on stellar temperature, were subtracted to convert bolometric magnitudes to absolute visual magnitudes, M_v . Then, applying the distance modulus:

$$m_v = M_v - 5 + 5 \log (d) \quad (3)$$

for 430 pc (parallax of 2.3248 milliarcseconds) gave the anticipated apparent magnitude (m_v) for each of the captured spectra.

These magnitudes are compared with their corresponding observed values in section 3.3.

3.2. Captured spectra: measurement of TiO transmittance and optical depth

To estimate the direct effects of atmospheric TiO in the range covered by our captured spectra, the levels of absorption across the specific TiO absorption bands in those spectra were examined. However, the level of the continuum in cool stars increases rapidly with increasing wavelength, especially so in the later M spectral classes; the required interpolation makes the measurement of depth across broad absorption bands difficult. A feature of `xCLASS`, included in its `XMK25` display routine and therefore implemented in the modified version `xCLASSMIRA`, is the ability to "rectify" the spectra; that is, to convert a flux-normalized spectrum to a spectrum with a fixed continuum set at unity, with the absorption value below the continuum for each wavelength correctly scaled in proportion. If the spectra are presented in an Excel spreadsheet as a list of each sampled wavelength and its corresponding amplitude, an individual wavelength or a wavelength group—such as a TiO band—may readily be selected for analysis. Thus, the absorption effects

Table 1. Luminosity and magnitudes calculated from spectra.

| <i>Obs. Date</i> | <i>Phase</i> | <i>Spectral Class</i> | <i>MK Temp. K</i> | <i>Luminosity W</i> | <i>M(bol)</i> | <i>Bol Conv.</i> | <i>M(v)</i> | <i>m(v)</i> |
|------------------|--------------|-----------------------|-------------------|---------------------|---------------|------------------|-------------|-------------|
| 07-May-19 | 0.97 | M0 IIIe | 3845 | 3.15E+29 | -2.55 | -1.25 | -1.30 | 6.87 |
| 26-May-19 | 0.18 | K7 IIIe | 3910 | 3.37E+29 | -2.62 | -1.09 | -1.53 | 6.64 |
| 30-May-19 | 0.22 | K5 IIIe | 3955 | 3.53E+29 | -2.67 | -1.00 | -1.67 | 6.50 |
| 03-Jun-19 | 0.26 | K8 IIIe | 3890 | 3.30E+29 | -2.60 | -1.13 | -1.47 | 6.70 |
| 09-Jun-19 | 0.33 | M1.5 IIIe | 3700 | 2.70E+29 | -2.38 | -1.64 | -0.74 | 7.43 |
| 13-Jun-19 | 0.37 | M2.2 IIIe | 3635 | 2.52E+29 | -2.31 | -1.81 | -0.50 | 7.67 |
| 17-Jun-19 | 0.42 | M3 IIIe | 3560 | 2.32E+29 | -2.22 | -2.00 | -0.22 | 7.95 |
| 22-Jun-19 | 0.47 | M4 IIIe | 3460 | 2.07E+29 | -2.09 | -2.24 | 0.15 | 8.32 |
| 02-Jul-19 | 0.58 | M4.5 III | 3408 | 1.95E+29 | -2.03 | -2.36 | 0.33 | 8.50 |
| 11-Jul-19 | 0.68 | M4.8 III | 3382 | 1.89E+29 | -1.99 | -2.40 | 0.41 | 8.58 |
| 15-Jul-19 | 0.73 | M4.6 III | 3397 | 1.92E+29 | -2.01 | -2.38 | 0.37 | 8.54 |
| 20-Jul-19 | 0.78 | M4.5 III | 3408 | 1.95E+29 | -2.03 | -2.36 | 0.33 | 8.50 |
| 23-Jul-19 | 0.82 | M4.2 IIIe | 3439 | 2.02E+29 | -2.06 | -2.30 | 0.24 | 8.40 |
| 26-Jul-19 | 0.85 | M3.2 IIIe | 3540 | 2.27E+29 | -2.19 | -2.05 | -0.14 | 8.03 |
| 29-Jul-19 | 0.88 | M2.5 IIIe | 3610 | 2.45E+29 | -2.28 | -1.88 | -0.40 | 7.77 |
| 02-Aug-19 | 0.93 | M2.2 IIIe | 3635 | 2.52E+29 | -2.31 | -1.81 | -0.50 | 7.67 |
| 05-Aug-19 | 0.96 | M2.1 IIIe | 3645 | 2.55E+29 | -2.32 | -1.78 | -0.54 | 7.63 |
| 12-Aug-19 | 0.04 | M2 IIIe | 3655 | 2.57E+29 | -2.33 | -1.76 | -0.57 | 7.60 |

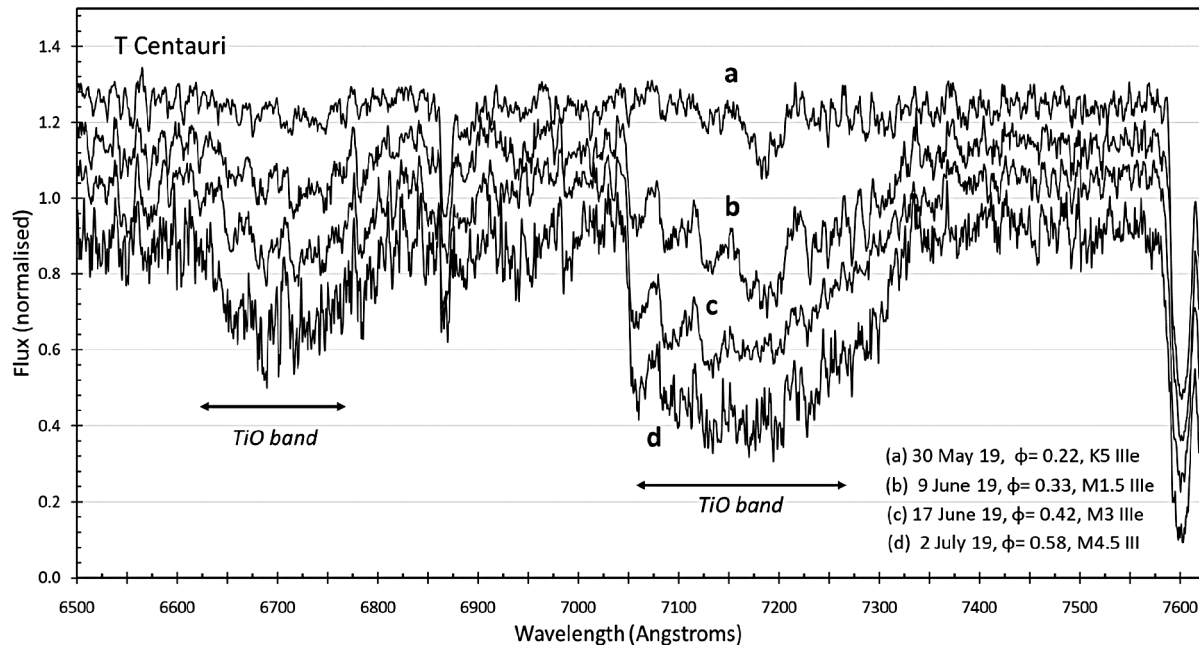


Figure 3. Example rectified spectra used for the measurement of the effect of TiO on atmospheric transmittance (with each continuum separated by 0.1 for clarity). The legend indicates phase and spectral type.

may be measured by selecting a wavelength range and taking the mean of those amplitudes relative to the continuum. The 18 spectra referenced in the tables were rectified, representing the entire period of T Cen under study; examples of those rectified spectra are presented in Figure 3.

As will be noted, the absorption by TiO occurs in clearly defined bands; these exist over much of the visual range, from $\lambda 4750$ onwards. The transmittance (defined as radiant flux transmitted/incident radiant flux) of the major TiO absorption band covering the wavelength range $\lambda \lambda 7054\text{--}7300$ was measured, wavelength by wavelength, over T Cen's period from the EXCEL spreadsheet. Also measured was the transmittance

of the wider wavelength range of $\lambda \lambda 6500\text{--}7500$, covering the majority of the recorded spectrum whilst avoiding the telluric O₂ absorption at $\lambda 7605$.

Also calculated was the optical depth of the absorption band, from:

$$\tau = -\ln T \quad (4)$$

where T is the Transmittance. Transmittance and optical depth are shown together in Figure 4 for both cases.

Optical depth reached a maximum of around 0.7 in the $\lambda \lambda 7054\text{--}7300$ TiO band at minimum light, confirming a

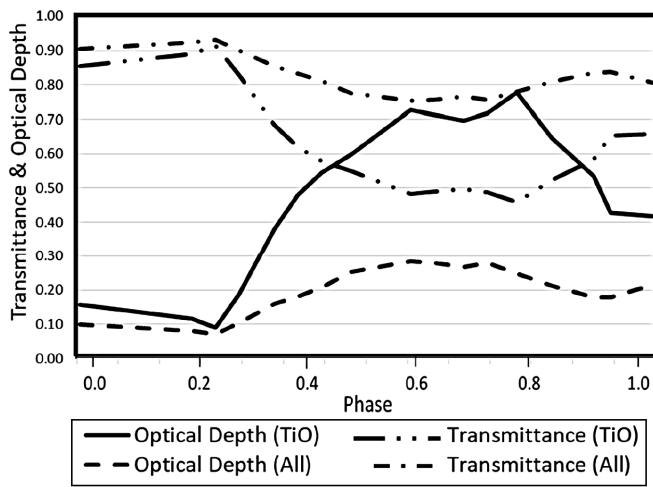


Figure 4. Transmittance and optical depth as measured from the rectified spectra. The plots designated “TiO” are for the absorption band $\lambda\lambda 7054\text{--}7300$; those designated “All” are for the wider spectral range, $\lambda\lambda 6500\text{--}7500$.

significant absorption of visible light within that band. This will also have occurred to a varying degree across the visible spectrum, as indicated by the curve for the wider wavelength range. Reid and Goldston (2002a, b) and Wing (1980) have adopted $\tau \geq 1$ as the requirement for atmospheric TiO to have formed a real “visual surface” above the true stellar surface represented by the photosphere. In the case of T Cen, this requirement was not met in full; nevertheless, the presence of significant quantities of molecular TiO in the extended atmosphere must create a structure—potentially complex—absorbing some of the emitted visual radiation and re-emitting it at longer wavelengths beyond the visual. If this structure—of layers, perhaps—is distant from the true stellar surface, it could well appear as a detectable increase in the effective stellar radius, together with a reduction in observed temperature and luminosity in the visual wavelength range. This potential increase in the apparent stellar radius, and its sensitivity to wavelength, is considered in section 3.4 and in section 4.

Table 2. Magnitudes of T Cen derived from AAVSO observations.

| <i>Obs. Date</i> | <i>Phase</i> | <i>Observed $m(v)$</i> | <i>Observed $M(v)$</i> | <i>Bol Conv.</i> | <i>M(bol)</i> | <i>Luminosity W</i> |
|------------------|--------------|-----------------------------------|-----------------------------------|------------------|---------------|----------------------------------|
| 07-May-19 | 0.97 | 6.30 | -1.87 | -1.25 | -3.12 | 5.32E+29 |
| 26-May-19 | 0.18 | 6.20 | -1.97 | -1.09 | -3.06 | 5.04E+29 |
| 30-May-19 | 0.22 | 6.25 | -1.92 | -1.00 | -2.92 | 4.43E+29 |
| 03-Jun-19 | 0.26 | 6.30 | -1.87 | -1.13 | -3.00 | 4.77E+29 |
| 09-Jun-19 | 0.33 | 6.55 | -1.62 | -1.64 | -3.26 | 6.06E+29 |
| 13-Jun-19 | 0.37 | 7.00 | -1.17 | -1.81 | -2.98 | 4.68E+29 |
| 17-Jun-19 | 0.42 | 7.20 | -0.97 | -2.00 | -2.97 | 4.64E+29 |
| 22-Jun-19 | 0.47 | 7.60 | -0.57 | -2.24 | -2.81 | 4.00E+29 |
| 02-Jul-19 | 0.58 | 8.10 | -0.07 | -2.36 | -2.43 | 2.82E+29 |
| 11-Jul-19 | 0.68 | 8.45 | 0.28 | -2.40 | -2.12 | 2.12E+29 |
| 15-Jul-19 | 0.73 | 8.20 | 0.03 | -2.38 | -2.35 | 2.62E+29 |
| 20-Jul-19 | 0.78 | 7.75 | -0.42 | -2.36 | -2.78 | 3.89E+29 |
| 23-Jul-19 | 0.82 | 7.45 | -0.72 | -2.30 | -3.02 | 4.86E+29 |
| 26-Jul-19 | 0.85 | 7.05 | -1.12 | -2.05 | -3.17 | 5.57E+29 |
| 29-Jul-19 | 0.88 | 6.85 | -1.32 | -1.88 | -3.20 | 5.73E+29 |
| 02-Aug-19 | 0.93 | 6.55 | -1.62 | -1.81 | -3.43 | 7.08E+29 |
| 05-Aug-19 | 0.96 | 6.45 | -1.72 | -1.78 | -3.50 | 7.55E+29 |
| 12-Aug-19 | 0.04 | 6.45 | -1.72 | -1.76 | -3.48 | 7.42E+29 |

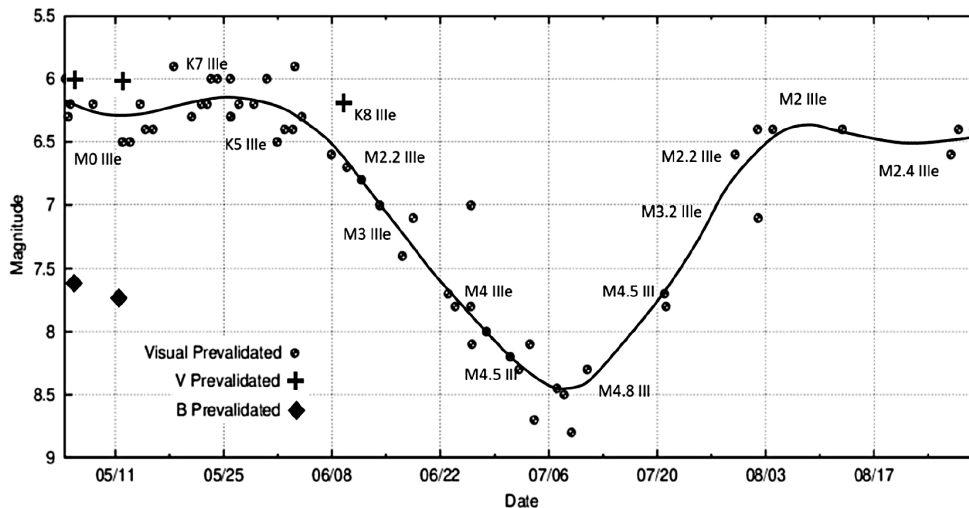


Figure 5. T Cen interpolated light curve (from a 12th order polynomial fit) with spectral classifications from XCLASSMIRA, covering the period studied (AAVSO data).

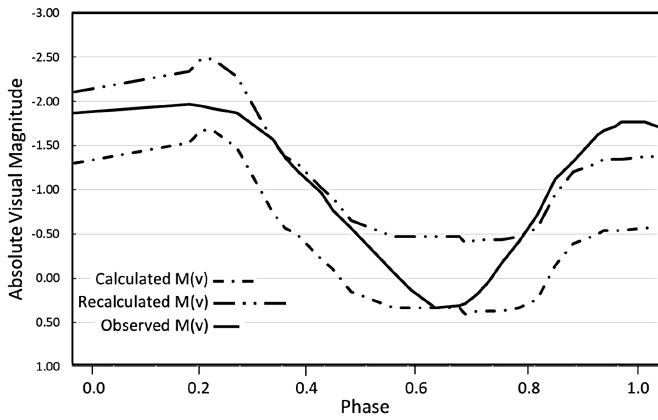


Figure 6. Original and recalculated absolute visual magnitudes from spectral data, compared with the observed values provided by the AAVSO. The recalculated values of M_v are based on the increased stellar radius of $94 R_\odot$.

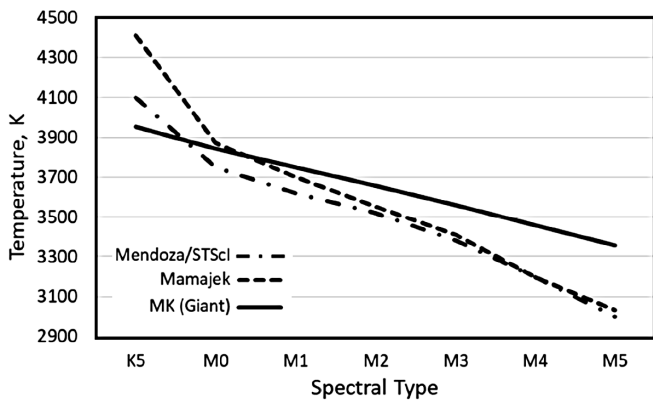


Figure 7. Comparison of (V–R) effective temperatures as compiled by Mamajek (2019) and Mendoza (1969)/STScI (2002), shown together with the MK standard effective temperatures for giant stars.

3.3. Derivation of photometric magnitudes

The next step was to compare the magnitudes derived from spectra with the observed magnitudes as published by the AAVSO.

The apparent visual magnitudes (m_v) of T Cen are shown in Figure 5, interpolated across the visual records using a 12th order polynomial fit to the purely visual measurements (using the AAVSO's VSTAR application (Benn 2013)). The figure has been annotated with the spectral classes identified for those dates, as determined in section 2.1.

To enable a thorough comparison with the luminosities and magnitudes calculated from the spectra, the observed apparent magnitudes were converted, using the same parameters as in section 3.1, to their absolute and bolometric magnitudes, and finally to luminosity, where:

$$L = L_\odot \times 10^{-M_{\text{Bol}}/2.51} \quad (5)$$

Again, $L_\odot = 3.0128 \times 10^{28}$ W (Mamajek *et al.* 2015).

Table 2 shows the AAVSO observed values of m_v for T Cen, together with their converted magnitudes and luminosities.

3.4. Reconciliation of calculated (from spectra) and observed magnitudes

Significant differences were apparent between the magnitudes calculated from the spectra and the AAVSO-observed magnitudes, which required explanation and resolution. The absolute visual magnitudes initially calculated from the spectral type (using the parameters outlined previously) and their AAVSO-observed counterparts are illustrated in Figure 6.

Despite having a similar shape, the curves only intersect at minimum brightness; it was considered, however, that the observed magnitudes were simply brighter than their calculated equivalents. To compare the behavior of T Cen from both the spectroscopic and photometric perspectives, it was necessary to bring the curves into much better alignment, to identify the key areas of difference. This entailed adjusting only the calculated values based on the spectra, as the observed absolute visual magnitudes were derived from many separate observations and were independent of any assumptions made or data used in the calculations. Both the assumed effective temperature and the effective stellar radius were reviewed to this end.

The effective temperatures used in calculating luminosity were the standard MK reference temperatures, as noted in section 3.1 (Gray and Corbally 2009), determined by spectral type. These are effectively the observed temperature of the stellar surface and may be more applicable to main sequence stars than to Miras and SRa stars on the Asymptotic Giant Branch. As the atmospheres of stars such as T Cen become obscured by molecules such as TiO as they cool, their observed temperatures may therefore be significantly lower than those prescribed by the MK model. Using the temperature to lift the calculated M_v curve into better alignment would have required increasing the temperatures above the MK giant values and would conflict with the overall structure of the MK temperature model. However, varying the radius alone would shift the calculated M_v curve without distorting it; this was preferred as the mechanism to improve the initial alignment of the two curves. A 45% increase, from the initial $65 R_\odot$ (4.5×10^{10} m) to $94 R_\odot$ (6.53×10^{10} m), was found to achieve the best fit, giving a revised stellar radius of ~ 0.44 AU, a not unreasonable size for a Mira variable (or similar) with a short period.

The revised calculated values of absolute visual magnitude, in comparison with the original and the observed values, are shown in Figure 6.

The improved alignment was not perfect, however, and differences persisted both in the early phases and around minimum light. The lower magnitudes observed by AAVSO contributors early in the period might have been due to molecular TiO, formed far from the true stellar surface, remaining in the atmosphere until dissociated either by the radiation from the star at its hottest spectral type or by shock waves induced by pulsation; following this, the magnitudes would be expected to converge as shown (Wing 1980). Alternatively, as the star pulsates, with its minimum photospheric radius estimated to occur at $\phi \sim 0.8$, it may be that the expansion prior to $\phi = 0$ reduced the temperature, and hence the luminosity. These issues are considered further in section 4.

At minimum light ($\phi \sim 0.63$), a full magnitude difference remained between the values of M_v derived from AAVSO observations and those recalculated based on spectral type and

the larger radius. At this stage in the period, TiO is expected to increase towards its maximum in the atmosphere, absorbing radiation within its absorption bands, and reducing T Cen’s visual brightness and observed temperature. As noted in section 3.2, the TiO absorption evident in our captured spectra confirmed significant levels of absorption in these bands around minimum light, giving rise to these lower observed magnitudes, and potentially increasing its apparent radius.

It was suspected, therefore, that in mid-phase the MK standard temperatures, although falling mid-period according to spectral type, did not accurately represent the external appearance of the complex atmosphere of a pulsating giant star such as a Mira (or similar). The atmosphere is not only enormous but may have widely different structure and temperatures at different depths (Hinkle and Barnes 1979, cited by Wing 1980); hence, whilst the MK temperatures may be appropriate for the photosphere itself, other methods—such as the well-established use of color indices—may give a better indication of the cooler conditions farther out, which affect the visual magnitudes. The B–V color index-temperature relationship appeared to be of lesser value for cool stars, given that much of the radiation is in the infra-red, and varies significantly with spectral type. The use of the V–R color index to refine the effective temperature of T Cen was therefore investigated and two relationships were found between effective temperature and the V–R color index. First, a comprehensive table of spectral types, temperatures, and a wide range of color indices compiled by Mamajek (2019) offered a set of spectral types and associated effective temperatures that could be applied in this model, although the data relate to dwarf stars.

Second, a paper by Mendoza (1969) linked V–R indices (originally $(V-R)_j$) to effective temperature based on observations of stars with a range of luminosities, including several giants; applying these $(V-R)_j$ indices to the extensive table linking color indices and spectral types published by the Space Telescope Science Institute (2002), gave another set of spectral types and corresponding effective temperatures.

The two sets of data, plotted in Figure 7, showed considerable similarity, especially at minimum light, but diverge towards spectral type K5. For the transition M0 to K5, Mamajek’s temperatures show a significantly greater increase than the Mendoza/STScI interpretation.

Also shown in Figure 7 is the MK temperature sequence for giant stars of luminosity type III (Gray and Corbally 2009), which remains above both the (V–R) curves from M0 to M5 as the atmosphere cools and becomes obscured by TiO. Between K5 and M0, however, the MK temperature for giants remains below both (V–R) projections; this is consistent with the MK effective temperature calibration for late-type stars (Gray and Corbally 2009), in which giants of type G and K are shown to be significantly cooler than their dwarf counterparts. The rapid rise in temperature in the Mamajek study plainly follows the behavior of dwarf stars once the atmosphere is clear of molecules such as TiO; the lesser rise in the Mendoza/STScI temperatures, extending almost as far as M2, is probably attributable to Mendoza’s inclusion of giant stars (Mendoza 1969).

Gray and Corbally refer specifically to this spectroscopic transition in their discussion of the classification of M-type stars

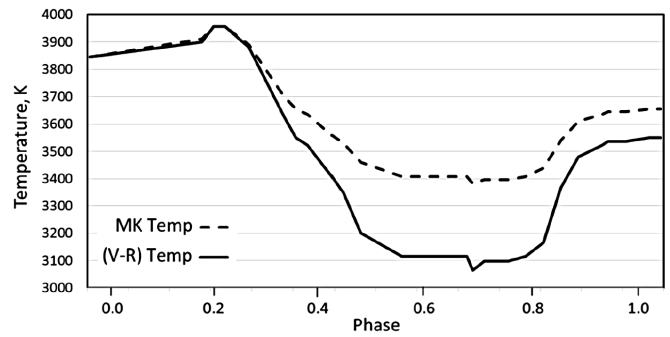


Figure 8. Combined MK and Mamajek (V–R) temperatures compared to the MK standard values for giant stars (applied to the spectral classifications across the period).

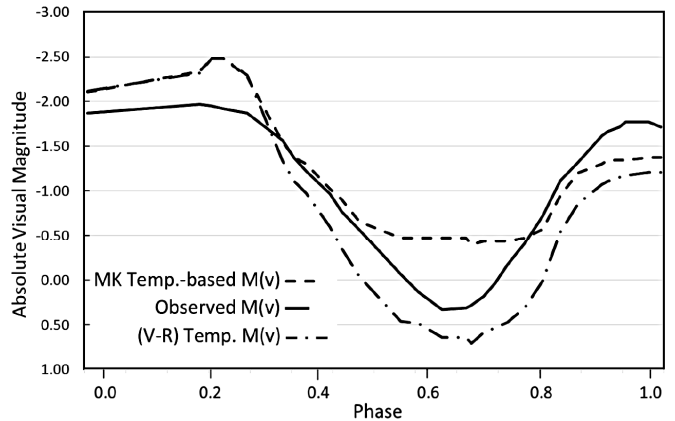


Figure 9. Comparison of the absolute visual magnitudes: Observed values are the AAVSO observed values; MK Temp.-based magnitudes are those derived from spectral data (using MK standard temperatures and the increased radius of $94 R_{\odot}$); (V–R) Temp. magnitudes are based on the combination of both the MK-based standard temperatures and the (V–R)-derived (Mamajek) temperatures of Table 3 and Figure 9, also with the increased radius of $94 R_{\odot}$.

(Gray and Corbally 2009, sec. 8.2.2 and their footnote No. 1), and state that “in terms of effective temperature, the jump from K5 to M0 is small, and is comparable to that between M0 and M1.” The K5–M0 region is when T Cen is brightest and its atmosphere is least obscured, based on the absence of TiO in the spectra; it may be assumed that the effective temperature should then be closest to the MK standard for giant stars. In developing our simplified model of T Cen’s behavior, those MK (giant) temperatures were adopted for spectral types from K5 to M0, and Mamajek’s more recent temperatures were applied thereafter; these are listed in Table 3 and are shown in

Table 3. Spectral type and effective temperature (based on MK temperatures for giant stars and Mamajek’s (2019) color index data).

| Spectral Class | Effective Temp. K |
|----------------|-------------------|
| K5 | 3955 |
| M0 | 3845 |
| M1 | 3700 |
| M2 | 3550 |
| M3 | 3410 |
| M4 | 3200 |
| M5 | 3030 |

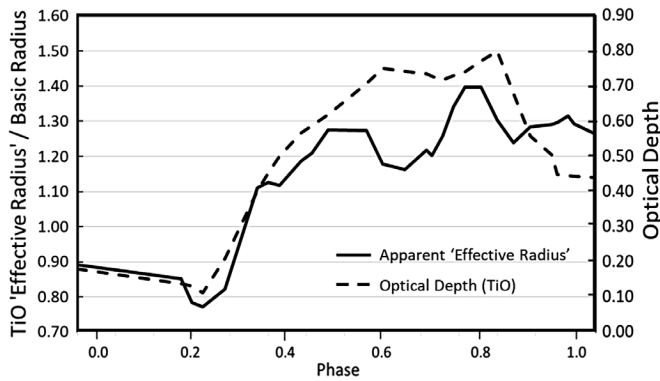


Figure 10. Estimated ratio of the “effective radius” of T Cen, increased due to atmospheric TiO, relative to the assumed “basic radius” of $94 R_{\odot}$ (left axis); also illustrated is the optical depth of the TiO absorption band $\lambda\lambda 7054\text{--}7300$ (right axis).

Figure 8 as they apply to the spectral types across the period; the temperatures were interpolated linearly for intermediate spectral types. The corresponding MK standard temperatures for giant stars are also shown in Figure 8.

These (V-R) temperatures were then applied in the standard Stefan-Boltzmann formula (Equation 1), using the previously increased assumed stellar radius of $94 R_{\odot}$, to recalculate revised luminosities and bolometric magnitudes. Prior to determining the visual magnitudes, the bolometric conversion factors were plotted and corrected to match the effective temperatures now being applied. The results are shown in Table 4 and in Figure 9; for clarity, “(V-R)” precedes references to the applied temperatures, and to other values dependent on them.

The values for M_v based on the combined temperature sequence (incorporating both MK standard and Mamajek (V-R) values) were largely as expected, with the temperatures in the early and late phases not unlike those previously calculated. Toward minimum light, however, the values are fainter than the AAVSO observed values, as expected for a cool outer atmosphere significantly obscured by TiO, but where the

expected increase in the apparent “effective radius” due to the atmospheric TiO has not yet been incorporated into the calculation of luminosity. These differences in magnitude now offered an opportunity to assess the apparent increase of the TiO “surface” and how it varied during T Cen’s cycle, as a form of proxy for the undoubted complexity of the real atmospheric structure, in which the observed “disk radius” is itself wavelength-dependent.

The scale of this increase in apparent “effective radius” may be approximated by calculating the ratio of the radii from the Stefan-Boltzmann formula (Equation 1), using the absolute visual magnitude as representing the luminosity in the visual range. If the effective temperatures, for both the observed and (V-R) cases, are assumed to be the same, the ratio of the radii may be calculated as follows:

$$R_{(V-R)} / R_{(Observed)} = (2.51^{\Delta M})^{1/2} \quad (6)$$

where

$$\Delta M = M_{V(V-R)} - M_{V(Observed)} \quad (7)$$

Applying this to the magnitudes quoted in Table 4 gives the curve shown in Figure 10.

Based on this modelling, the apparent “effective radius” of T Cen increased by between 20–30%, with a brief maximum of 40% above the (previously enlarged) radius assumed for the photosphere ($94 R_{\odot}$). The rise commenced at $\phi \sim 0.25$ and decreased again after $\phi \sim 0.8$. The general shape of the variation in apparent radius is consistent with the increase in optical depth, also shown in Figure 10, inferring a clear relationship with the appearance and increase of TiO in T Cen’s atmosphere. The apparent radius measurements also show similar characteristics to those taken for Mira (o Ceti) itself, including the significant dip at around $\phi \sim 0.6$, although Mira’s variation was significantly greater (Mahler *et al.* 1997). The values of less than one occurring up to $\phi \sim 0.3$ result from the

Table 4. Luminosities and magnitudes based on the (V-R) temperatures.

| Obs. Date | Phase Class | Spectral K | (V-R) Temp. W | (V-R) Lum. M(bol) | (V-R) | Bol Conv. M(v) | (V-R) M(v) | (V-R) |
|-----------|-------------|------------|---------------|-------------------|-------|----------------|------------|-------|
| 07-May-19 | 0.97 | M0 IIIe | 3845 | 6.63E+29 | -3.36 | -1.50 | -1.86 | 6.31 |
| 26-May-19 | 0.18 | K7 IIIe | 3900 | 7.02E+29 | -3.42 | -1.35 | -2.07 | 6.10 |
| 30-May-19 | 0.22 | K5 IIIe | 3955 | 7.42E+29 | -3.48 | -1.10 | -2.38 | 5.79 |
| 03-Jun-19 | 0.26 | K8 IIIe | 3880 | 6.88E+29 | -3.40 | -1.45 | -1.95 | 6.22 |
| 09-Jun-19 | 0.33 | M1.5 IIIe | 3625 | 5.24E+29 | -3.10 | -1.90 | -1.20 | 6.97 |
| 13-Jun-19 | 0.37 | M2.2 IIIe | 3522 | 4.67E+29 | -2.98 | -2.10 | -0.88 | 7.29 |
| 17-Jun-19 | 0.42 | M3 IIIe | 3410 | 4.10E+29 | -2.84 | -2.40 | -0.44 | 7.73 |
| 22-Jun-19 | 0.47 | M4 IIIe | 3200 | 3.18E+29 | -2.56 | -2.55 | -0.01 | 8.16 |
| 02-Jul-19 | 0.58 | M4.5 III | 3115 | 2.86E+29 | -2.44 | -3.00 | 0.56 | 8.73 |
| 11-Jul-19 | 0.68 | M4.8 III | 3064 | 2.67E+29 | -2.37 | -3.20 | 0.83 | 9.00 |
| 15-Jul-19 | 0.73 | M4.6 III | 3098 | 2.79E+29 | -2.42 | -3.05 | 0.63 | 8.80 |
| 20-Jul-19 | 0.78 | M4.5 III | 3115 | 2.86E+29 | -2.44 | -3.00 | 0.56 | 8.73 |
| 23-Jul-19 | 0.82 | M4.2 IIIe | 3166 | 3.05E+29 | -2.51 | -2.80 | 0.29 | 8.46 |
| 26-Jul-19 | 0.85 | M3.2 IIIe | 3368 | 3.90E+29 | -2.78 | -2.25 | -0.53 | 7.64 |
| 29-Jul-19 | 0.88 | M2.5 IIIe | 3480 | 4.45E+29 | -2.92 | -2.20 | -0.72 | 7.44 |
| 02-Aug-19 | 0.93 | M2.2 IIIe | 3522 | 4.67E+29 | -2.98 | -2.10 | -0.88 | 7.29 |
| 05-Aug-19 | 0.96 | M2.1 IIIe | 3536 | 4.74E+29 | -2.99 | -2.03 | -0.96 | 7.21 |
| 12-Aug-19 | 0.04 | M2 IIIe | 3550 | 4.82E+29 | -3.01 | -2.06 | -0.95 | 7.22 |

lower observed values of M_v relative to those calculated based on spectral type; this was noted earlier and is considered in more detail in section 4, as is the residual expansion remaining after $\phi \sim 0.9$.

The effective temperatures based on (V–R) data are essentially approximations linked to spectral type and were not otherwise derived from our observations; the estimated variations in effective radius should, therefore, only be considered as a simple model representation. T Cen has a relatively short period and a limited visual amplitude that does not extend as deeply into the M spectral types as do longer period Miras; nevertheless, the presence of an expanded apparent radius due to atmospheric TiO is clearly shown, and has a significant effect on the star’s behavior, especially in the visual range.

4. Discussion

4.1. Radius considerations

The dimensions of cool giant stars such as Miras are generally difficult to determine, especially during the cooler phases of their periods, when the atmosphere forms substantial amounts of metallic oxides such as TiO, VO, and others (Wing 1980). The obscuring effects of these oxides, which are themselves wavelength-dependent, have been described as both reducing the apparent temperature as viewed by an observer and increasing the apparent stellar radius (Reid and Goldston 2002a, b). Under such circumstances, however, a true stellar radius is not clearly visible, at least at most visual wavelengths, although interferometry is feasible in the infra-red (Weiner *et al.* 2003b; van Belle *et al.* 2002). The atmosphere itself is probably layered and subject to the effects of shock waves resulting from pulsation, both creating and eliminating molecules such as TiO, in addition to the effects of changing temperature (Höfner and Olofsson 2018). The concept here of an “effective radius” for T Cen is therefore a representation of the overall impact of TiO on the atmosphere for the purposes of developing what is sometimes referred to as an “embedded toy model” (Reutlinger *et al.* 2016), rather than an attempt to describe the physics in detail. Such a model may, however, potentially enable interesting comparisons to be made with the other Miras included in our wider study.

4.2. Estimation of basic stellar radius

At maximum brightness, T Cen exhibits as spectral type K5-K8 IIIe, with no spectroscopic indication of significant quantities of TiO in its atmosphere. With the photosphere clearly visible to an observer, its effective temperature was expected to be reasonably consistent with the MK standards for those spectral types. Thus, around maximum brightness, the luminosities and absolute visual magnitudes calculated using an assumed stellar radius should have approached those derived from the visual observations drawn from the records of the AAVSO. They did not, however, and varying the previously adopted stellar radius and recalculating the spectrum-based luminosities and magnitudes across the entire period, as described in Section 3.3, enabled the calculated and observed absolute visual magnitudes to be brought into significantly

better alignment. A 45% increase, from $65 R_\odot$ to $94 R_\odot$, was determined to give the best fit, giving a revised mean stellar radius of ~ 0.44 AU.

The period of a Mira variable has been described as primarily dependent upon its radius, and secondarily upon its mass (Percy 2007); indeed, Percy notes that the average radius of a Mira, in solar units, is approximately equal to its period in days so a radius of $94 R_\odot$ may be considered reasonable in this simple model for T Cen with its period of 91 days. However, the measured radii of Miras (and SRa stars) are dependent on wavelength, especially in the visual range when the atmosphere contains molecules such as TiO or VO. Interferometric measurements in the infrared have also given widely differing values for even the most extensively studied Miras, with the radius of Mira itself (o Ceti, period 332 days) being quoted as $\sim 350 R_\odot$ (Woodruff *et al.* 2004) and $\sim 475 R_\odot$ (van Belle *et al.* 2002). Other Miras have been given similarly broad estimates, so while our estimate of the mean radius of T Cen may pleasingly fit this assumption it must remain as an approximation for the purposes of our model, especially as T Cen appears only marginally to be a true Mira variable.

4.3. Consideration of Effective Temperature and radius variation

The anomaly created by the fainter observed magnitudes, and therefore lower effective temperatures (as opposed to the MK standard values) early in the cycle, up to $\phi \sim 0.25$ as illustrated in Figure 6, was considered to be due to either of two potential causes (or possibly a combination of both):

1. TiO formed far from the true stellar surface but remaining in the atmosphere until finally dissociated by the radiation from the star at its hottest spectral types, at which point the magnitudes would again converge. Wing (1980) indicates that this situation can occur and can last for a month or two after the photospheric temperature starts to approach maximum, which is reasonably consistent with this case. Had this been so, the observed magnitudes should have been brightening until $\phi \sim 0.2$ or even later, whereas having been relatively stable, they were now becoming steadily fainter. The absence of spectra between 2019 May 7–26 left an area of uncertainty in these early phases but from May 26 to June 3 the spectra showed no significant TiO absorption bands, so this interpretation was discounted at this stage.

2. Alternatively, it is probable that the star pulsates significantly, its radius changing by perhaps $\pm 10\%$ (Weiner *et al.* 2003a), with a noticeable effect on luminosity, although in the absence of information confirming the nature of pulsation by T Cen, this was ignored in our initial estimate of T Cen’s radius. As the star pulsates, its minimum photospheric radius probably occurs around $\phi \sim 0.8$, as indicated by the onset of emission at H α due to the likely development of outward shockwaves as expansion commences, and the radial velocity variations shown by Lebzelter *et al.* (2005). It was possible, therefore, that the actual effective temperature differed from the MK standard, which we presumed related to stars in a steady state. As pulsating stars should cool as they expand (albeit

with a small delay between minimum radius and maximum brightness), it was thought possible that the star might be somewhat cooler by the time the phase reached $\phi \sim 0$. However, to investigate the timing and degree of pulsation requires spectra capable of yielding radial velocities and is therefore beyond the scope of this paper.

The potential that the MK standard temperatures might not apply directly to a pulsating star, together with the difference of a full magnitude between the calculated and observed M_V values at minimum brightness, raised the possibility that a different method should be applied to determine the effective temperature, at least around minimum light. Color indices are commonly used to estimate stellar temperatures and, as has been described in section 3.3, the V–R relationship appeared to be more suitable for cool stars, given that much of the radiation is in the infra-red and varies significantly in the later M spectral classifications. The identification of a range of temperatures to be incorporated into our simplified model of T Cen’s behavior has been described in section 3.3; the MK (giant) temperatures were adopted for spectral types from K5 to M0, and Mamajek’s sequence of temperatures was applied thereafter into the M classifications.

This sequence of effective temperatures yielded calculated magnitudes much better aligned to those observed for T Cen, especially mid-period, and enabled an estimate to be made of the degree of apparent expansion of T Cen’s radius related to the TiO in its atmosphere. As noted above, this apparent “effective radius” is intended solely as a representation of the overall effect of TiO in T Cen’s atmosphere; further, as these temperatures were based on externally sourced data not captured directly from our own observations of T Cen, the derived variations in effective radius should only be considered as approximate. As described in section 3.3, the estimated increase in the “effective radius” was of the order of 20–30%, commencing at $\phi \sim 0.25$, and peaking at 40% above the estimated photospheric radius of $94 R_{\odot}$. T Cen has a relatively short period compared with most Miras or SRa stars; it also descends appreciably less into the later M spectral classes than true Miras. The opacity of the atmospheric TiO may, therefore, be expected to be less than that for longer period Miras, in which the apparent radius may double (or more). Nevertheless, it is clear that T Cen does develop some form of exterior “visual surface” in mid-period, although its true structure may well be complex and a limited study such as this cannot determine it. The presence of an expanded apparent “effective radius” due to molecular TiO is clearly shown, however, and has a significant effect on the star’s behavior, especially in the visual range.

During the later phases of the cycle, the captured spectra clearly showed that the atmosphere of T Cen retains some TiO, at least in this cycle; its spectral type stabilized at around M2 IIIe rather than rising to the previous K5–K8 IIIe, and its optical depth remained at $\tau \sim 0.44$. As pulsation may vary from cycle to cycle, a reduced incidence of shockwaves in the case under study may have led to TiO remaining in the atmosphere for longer than in other cycles, whereas a more vigorous pulsation may accelerate the dissociation of TiO and T Cen’s return to spectral type K. A review of T Cen’s light curve across several

91-day cycles (Figure 2) shows a considerable variation in peak brightness and in amplitude, leading to the conclusion that this situation is not unusual. It may be, therefore, that the fundamental period of T Cen is longer—181 days is commonly suggested—but with a first overtone perhaps governing much of its behavior. Determination of this would require detailed analysis over a much longer period and has not been considered here.

Note: Original copies of these spectra in .fit format may be accessed through the AAVSO ftp site at

<ftp://ftp.aavso.org/public/datasets/west491-fitsspectra.zip>.

5. Acknowledgements

We acknowledge with thanks the variable star observations for T Cen from the AAVSO International Database, contributed by observers worldwide and used in this research.

We thank Prof. Richard O. Gray (Appalachian State University, NC) for providing the XCLASS program and its standard databases, and in addition we express our appreciation to both him and Dr. Christopher Corbally S. J. (Vatican Observatory), for their kind support in its use. We also thank fellow members of the Astronomical Association of Queensland for their contributions in reviewing and advising on the content of this paper. We further thank both the editorial staff at JAAVSO for their support, and the anonymous referee who provided a careful review and valuable recommendations for this paper.

We acknowledge with thanks a grant from the Edward Corbould Research Fund, of the Astronomical Association of Queensland, for the purchase of a spectrograph, gratings, and CCD camera.

References

- Benn, D. 2013, VSTAR data analysis software (<https://www.aavso.org/vstar-overview>).
- Buil, C. 2019, ISIS: Integrated Spectrographic Innovative Software (<http://www.astrosurf.com/buil/isis-software.html>).
- Gray, R. O., and Corbally, C. J. 2009, *Stellar Spectral Classification*, Princeton Univ. Press, Princeton, NJ.
- Gray, R. O., and Corbally, C. J. 2014, *Astron. J.*, **147**, 80.
- Hinkle, K. H. and Barnes, T. G. 1979, *Astrophys. J.*, **227**, 923.
- Höfner, S., and Olofsson, H. 2018, *Astron. Astrophys. Rev.*, **26**, 1 (<https://doi.org/10.1007/s00159-017-0106-5>).
- Kafka, S. 2020, variable star observations from the AAVSO International Database (<https://www.aavso.org/aavso-international-database-aid>).
- Kaler, J. B. 1989, *Stars and their Spectra: An Introduction to the Spectral Sequence*, Cambridge Univ. Press, Cambridge, 263.
- Lançon, A., and Mouhcine, M. 2002, *Astron. Astrophys.*, **393**, 167.
- Lançon, A., and Wood P. R. 2000, *Astron. Astrophys., Suppl. Ser.*, **146**, 217.
- Lebzelter, T., Hinkle K. H., Wood P. R., Joyce R. R., and Fekel F. C. 2005, *Astron. Astrophys.*, **431**, 623.

- Mahler, T. A., Wasatonic, R., and Guinan, E. F. 1997, *Inf. Bull. Var. Stars*, No. 4500, 1.
- Mamajek, E. 2019, "A Modern Mean Dwarf Stellar Color and Effective Temperature Sequence" (2019.03.22 version used; http://www.pas.rochester.edu/~emamajek/EEM_dwarf_UBVIJHK_colors_Teff.txt (2021.0302 version)).
- Mamajek, E. E., *et al.* 2015, "IAU 2015 Resolution B2 on Recommended Zero Points for the Absolute and Apparent Bolometric Magnitude Scales," XXIXth IAU General Assembly in Honolulu, 13 August 2015 (<https://www.iau.org/administration/resolutions/>).
- Mendoza v., E. E. 1969, in *Proceedings of the 3rd Harvard-Smithsonian Conference on Stellar Atmospheres*, ed. O. Gingerich, Massachusetts Institute of Technology, Cambridge, MA, 27.
- Percy, J. R. 2007, *Understanding Variable Stars*, Cambridge University Press, Cambridge, 209–.
- Reid, M. J., and Goldston, J. E. 2002a, *Astrophys. J.*, **568**, 931.
- Reid, M. J., and Goldston, J. E. 2002b, *Astrophys. J.*, **572**, 694 (erratum).
- Reutlinger, A., Hangleiter, D., and Hartmann, S. 2018, *Br. J. Philos. Sci.*, **69**, 1069.
- Samus, N. N., Kazarovets, E. V., Durlevich, O. V., Kireeva, N. N., and Pastukhova, E. N. 2017, *Astron. Rep.*, **61**, 80, *General Catalogue of Variable Stars: Version GCVS 5.1* (<http://www.sai.msu.su/gcvs/gcvs/index.htm>).
- Space Telescope Science Institute. 2002, "Intrinsic Colours as a Function of Spectral Type" (<https://www.stsci.edu/~inr/intrins.html>).
- Universe Guide. 2020, T Cen (<https://www.universeguide.com/star/66825/tcentauri>).
- van Belle, G. T., Thompson, R. R., and Creech-Eakman, M. J. 2002, *Astron. J.*, **124**, 1706.
- Weiner, J, Hale, D. D. S., and Townes, C. H. 2003a, *Astrophys. J.*, **588**, 1064.
- Weiner, J, Hale, D. D. S., and Townes, C. H. 2003b, *Astrophys. J.*, **589**, 976.
- Wenger, M., *et al.* 2000, *Astron. Astrophys., Suppl. Ser.*, **143**, 9. (<http://simbad.u-strasbg.fr/simbad>).
- Wing, R. F. 1980, in *NASA. Goddard Space Flight Center Current Problems in Stellar Pulsation Instabilities*, 533 (<https://core.ac.uk/reader/42864826>).
- Woodruff, H. C., *et al.* 2004, *Astron. Astrophys.*, **421**, 703.

Appendix: Spectra used in this paper

These spectra in .fit format may be accessed through the AAVSO ftp site at <ftp://ftp.aavso.org/public/datasets/west491-fitspectra.zip>.

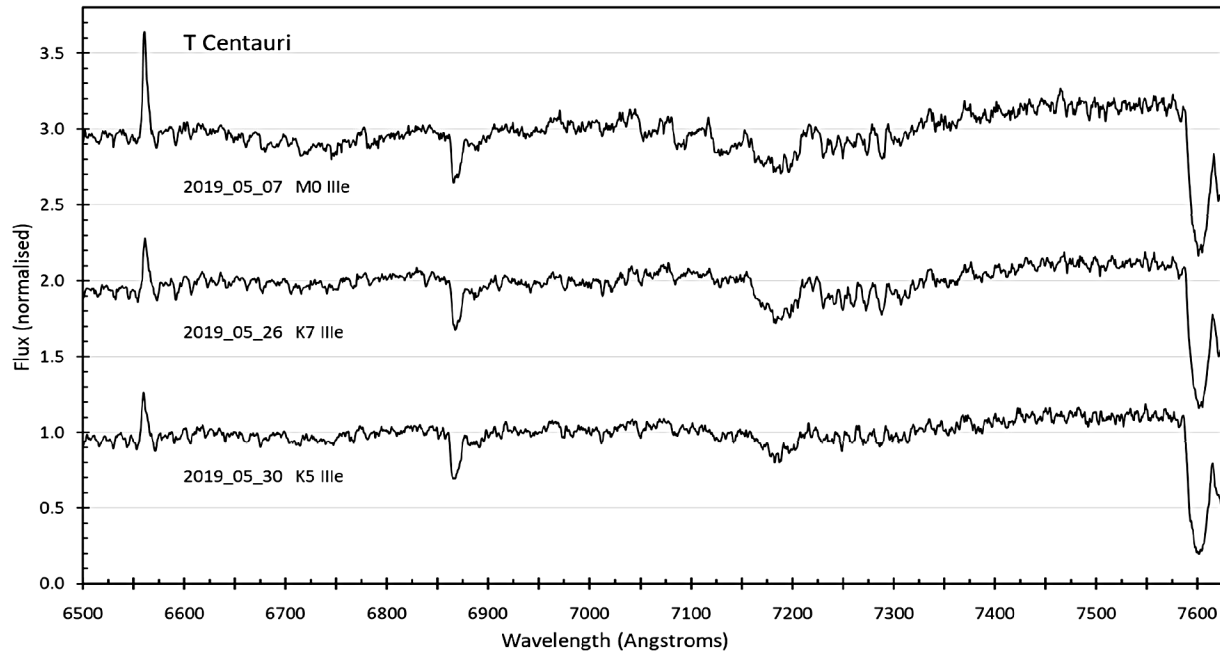


Figure A1. Spectra of $\lambda\lambda 6500\text{--}7630$, from the dates shown and at phases 0.97 (-0.03 of the studied period), 0.18, and 0.22 respectively, normalized at $\lambda 6610$; the profiles are separated by amplitude 1.0 for clarity.

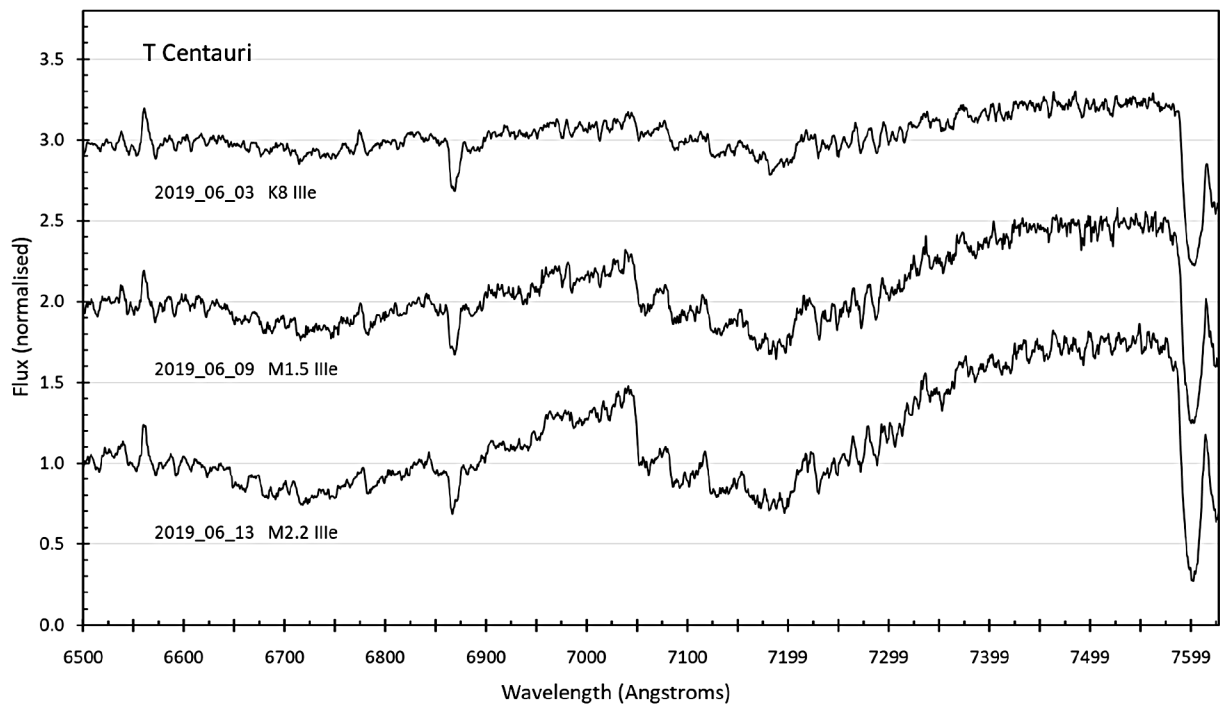


Figure A2. Spectra of $\lambda\lambda 6500\text{--}7630$, from the dates shown and at phases 0.26, 0.33, and 0.37 respectively, normalized at $\lambda 6610$; the profiles are separated by amplitude 1.0 for clarity.

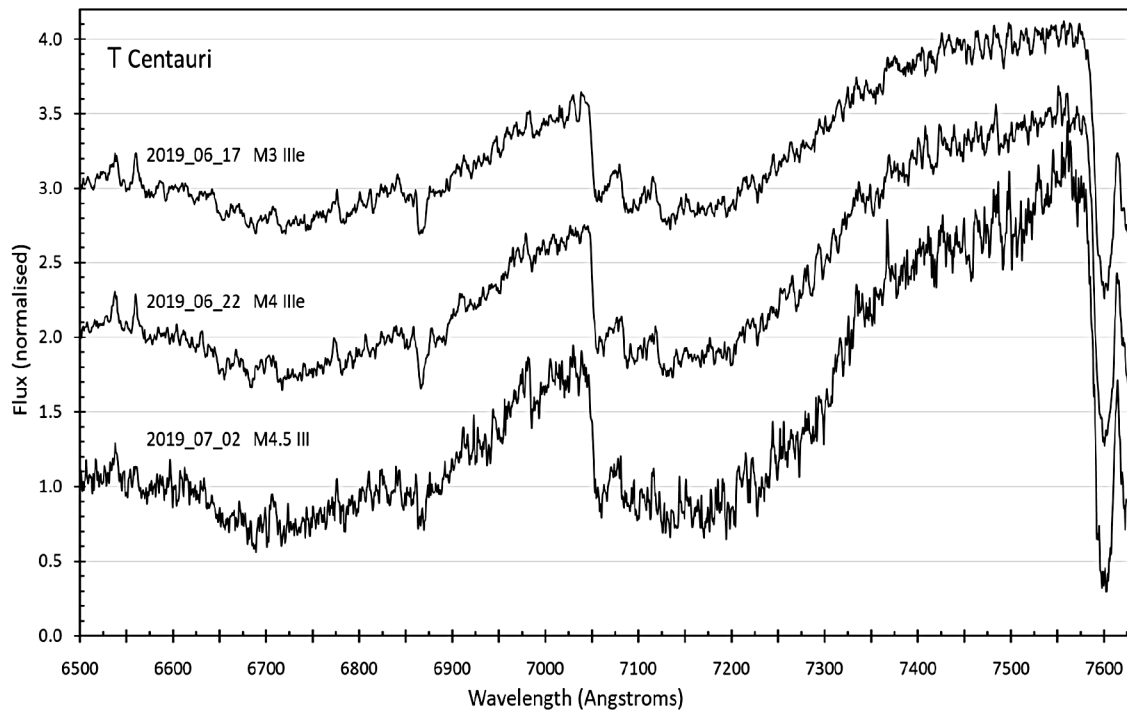


Figure A3. Spectra of $\lambda\lambda$ 6500–7630, from the dates shown and at phases 0.42, 0.47, and 0.58 respectively, normalized at λ 6610; the profiles are separated by amplitude 1.0 for clarity.

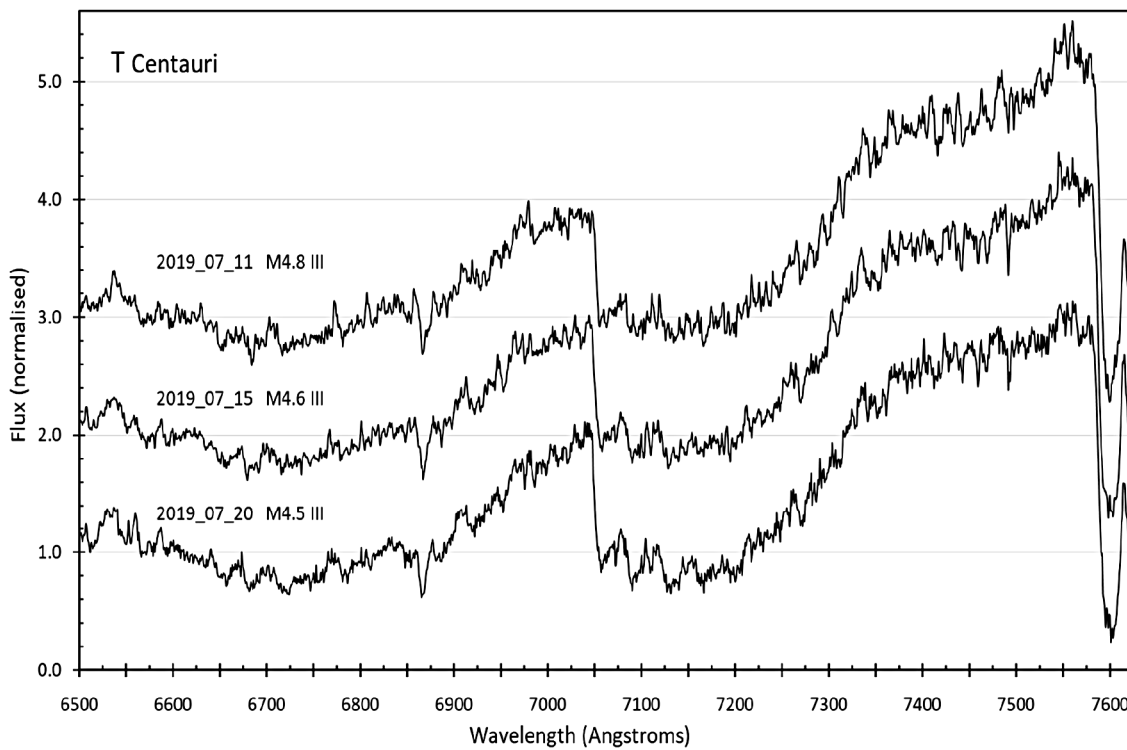


Figure A4. Spectra of $\lambda\lambda$ 6500–7630, from the dates shown and at phases 0.68, 0.73, and 0.78 respectively, normalized at λ 6610; the profiles are separated by amplitude 1.0 for clarity.

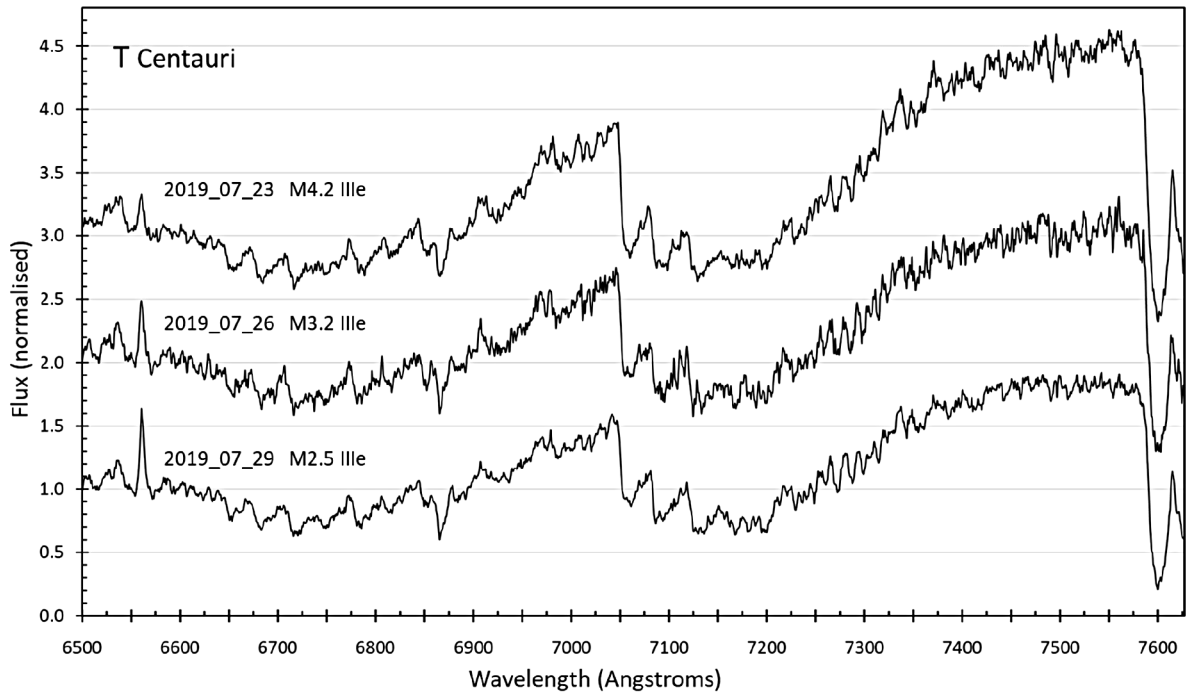


Figure A5. Spectra of $\lambda\lambda$ 6500–7630, from the dates shown and at phases 0.82, 0.85, and 0.88 respectively, normalized at λ 6610; the profiles are separated by amplitude 1.0 for clarity.

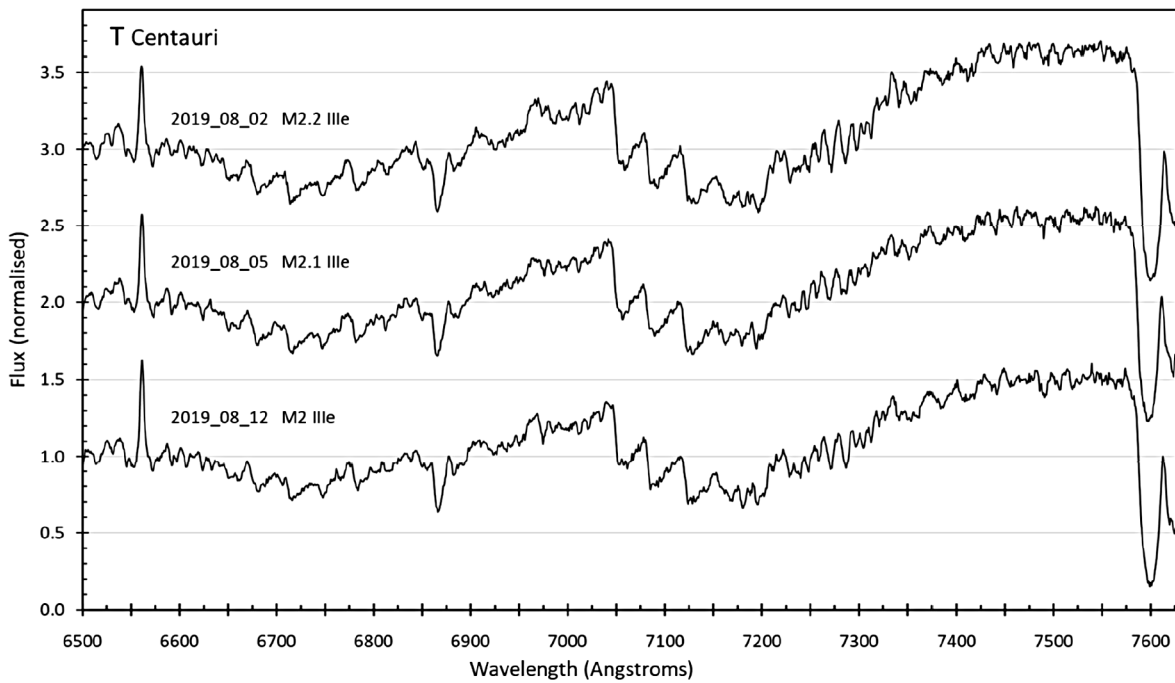


Figure A6. Spectra of $\lambda\lambda$ 6500–7630, from the dates shown and at phases 0.93, 0.96, and 0.04 (1.04 in the following period) respectively, normalized at λ 6610; the profiles are separated by amplitude 1.0 for clarity.